Multimodal luminescent $Yb^{3+}/Er^{3+}/Bi^{3+}$-doped perovskite single crystal for X-ray detection and anti-counterfeiting

Zhichao Zeng, Bolong Huang, Xia Wang, Lu Lu, Qiuyang Lu, Mingzi Sun, Tong Wu, Tengfei Ma, Jun Xu, Yueshan Xu, Shuao Wang, Yaping Du* and Chun-Hua Yan*

Z. Zeng, T. Ma, Dr. J. Xu, Y. Xu, Prof. Y. Du, Prof. C.-H. Yan
Tianjin Key Lab for Rare Earth Materials and Applications, Center for Rare Earth and Inorganic Functional Materials, School of Materials Science and Engineering, National Institute for Advanced Materials, Nankai University, Tianjin 300350, China
E-mail: ypdu@nankai.edu.cn

L. Lu, Q. Lu, M. Sun, T. Wu, Prof. B. Huang
Department of Applied Biology and Chemical Technology, The Hong Kong Polytechnic University, Hung Hom, Kowloon, Hong Kong SAR, China
E-mail: bhuang@polyu.edu.hk

X. Wang, S. Wang
State Key Laboratory of Radiation Medicine and Protection, School for Radiological and Interdisciplinary Sciences (RAD-X) and Collaborative Innovation, Center of Radiation Medicine of Jiangsu Higher Education Institutions, Soochow University, 199 Ren'ai Road, Suzhou 215123, China

Prof. C.-H. Yan
Beijing National Laboratory for Molecular Sciences, State Key Laboratory of Rare Earth Materials, Chemistry and Applications, PKU-HKU Joint Laboratory in Rare Earth Materials and Bioinorganic Chemistry, College of Chemistry and Molecular Engineering, Peking University, Beijing 100871, China

Prof. C.-H. Yan
College of Chemistry and Chemical Engineering, Lanzhou University, Lanzhou 730000, China

Keywords: Double perovskite, Multi-modal luminescence, Rare earth, X-ray detection, Anti-counterfeiting

The anticounterfeiting techniques have become the global topic since it is correlated to the information and data safety, in which the multimodal luminescence has been one of the most desirable candidates for practical applications. However, it is a long-standing challenge to actualize the robust multimodal luminescence with high thermal stability and humid resistance. Conventionally, the multimodal luminescence is usually achieved by the combination of up-conversion and downshifting luminescence, which only responds to the electromagnetic waves in a limited range. Herein, the $Yb^{3+}/Er^{3+}/Bi^{3+}$ co-doped $Cs_2Ag_{0.6}Na_{0.4}InCl_6$ perovskite material as the efficient multimodal luminescence material has been reported. Beyond the excitation of

ultraviolet light and near-infrared laser (980 nm), this work extends the multimodal luminescence to the excitation of *X*-ray for the first time. Besides the flexible excitation sources, this material also shows the exceptional luminescence performance, in which the detection limit of *X*-ray reaches the level of nGy/s, indicating a great potential for further application as a colorless pigment in the anti-counterfeiting field. More importantly, the obtained double perovskite features high stability against both humidity and temperature up to 400 °C. This integrated multifunctional luminescent material provides a new directional solution for the development of multifunctional optical materials and devices.

The counterfeiting issue has become a serious global problem involving every aspect of everyone's daily life such as banknotes, artworks, documents, and even personal information safety. To solve this issue, various technologies have been developed in the past decades including the plasmon, magnetism, luminescence, and also the recent hologram technique [1-3]. Compared to other conventional techniques, the fluorescence printing patterns supply promising high security to the key information valuable documents due to the tunable emission properties [4,5]. As counterfeiting technology has also been quickly developed, the traditional mono-mode anticounterfeiting is far from the requirement of practical applications to guarantee a high level of data and information safety. The traditional anti-counterfeiting luminescence is achieved by the mono-mode down-shifting (DS) luminescence, which converts the high energy photon into lower energy luminescence. To address such concern, developing more complicated anticounterfeiting techniques by increasing the luminescent modes becomes the most challenging topic. Presently, the realization of concurrent up-conversion (UC) and DS have been successfully utilized in anti-counterfeiting based on the lanthanide-based dopants [6-9]. The Eu-doped down-shift luminescent materials have been applied in the Euro banknotes, which enables the visible photoluminescence based on UV lamp excitation. Meanwhile, the

BANK OF CHINA also introduced the Yb/Er-doped UC phosphors in the banknotes as the counterfeiting technique, which emits the yellow UC luminescence by the irradiation of 980 nm laser. Meanwhile, the thermoluminescence and mechanoluminescence have also been introduced to the combination of DS and UC to upgrade the dual-modal luminescence technique to triple-modal luminescence with increased anticounterfeiting levels [10,11]. Besides the multimodal requirements, high stability is another key issue for the practical application of the anticounterfeiting materials. In particular, for the perovskite materials, the high thermal stability and resistance to the humidity of the environment have been a long-term issue. Therefore, how to realize the appropriate combination of both multimodal luminescence and high stability under harsh environment is the key to maximally improve the anticounterfeiting level of the materials.

For the selection of materials to realize the multimodal luminescence, some rare earth (RE) ions (such as Yb^{3+} and Nd^{3+}) have been intensively studied due to their unique 4*f* electronic configurations and energy-level structures.[12] For example, Yb^{3+} can absorb NIR light at 980 nm and transfer the energy to luminescent center ions (such as Ho^{3+}, Er^{3+}, Tm^{3+}), which in turn emit luminescence, completing the UC photoluminescence (PL) process.[13] Although a vast number of compounds can absorb ultraviolet light, only a few classes among them, such as quantum dots, perovskite materials, organic molecules, etc., can emit luminescence.[14,15] As for the XEL materials, heavy atoms are the typical selection, which emits the low-energy visible light via a series of complex photo-physical conversion processes.[16,17] In order to achieve the ultimate goal of multimodal luminescent performance, it is necessary to systematically integrate various luminescence properties from combining luminescent materials, RE ions and other metal ions.[18,19] Until now, it is a challenging task to find suitable matrices and elements to successfully actualize such a combination strategy for this multi-purpose luminescence.[20] As known, most of the matrices for RE-based UC materials are oxides or fluorides, in which DS

PL is rarely achievable.[21] For DS materials like quantum dots, doping RE ions is rather difficult.[22] And it is also difficult to combine organic molecules with RE ions to simultaneously realize UC and DS PL.[23] In recent years, some lead cesium halide based perovskite materials with RE dopants realize UC and DS PL, which can serve as the ideal candidates for multimodal luminescent materials.[24] More importantly, the DS PL and X-ray-excited luminescence (XEL) perovskite materials have been studied in recent reports.[25] However, these halides perovskite materials contain toxic lead ions with poor stability against high-temperature, humidity and oxygen. These shortcomings not only limit their durable and large-scale applications but also bring potential pollution sources to the environment.[24],[26] Therefore, developing stable lead-free multimodal luminescent materials have become an urgent task for the scientific community. Researchers recently reported that some lead-free double perovskite materials have excellent optical properties and good stabilities, such as $Cs_2AgBi(In,Sb)Cl_6$.[27,28] Recently, Zhu et al. have also reported the flexible control of the X-ray imaging performances through the Bi doping in $Cs_2Ag_{0.6}Na_{0.4}BiInCl_6$, supporting the competitive scintillation performances of the lead-free halide double perovskites [29]. Such types of perovskite containing strong binding force from chlorine and silver ions, which further improve their stability against high temperature and oxygen.[30] Moreover, those silver-containing perovskite halide materials comprise trivalent metal ions, such as Sb^{3+}, Bi^{3+} and In^{3+}, which have the same valence state and similar ionic radii with RE ions, indicating the facile doping process and slight influence on the lattice structure.[31] The crystallographic sites of these trivalent ions can be readily replaced by RE ions.[32] In previous works, the introduction of RE ions is able to promote the tuning of the emission upon X-ray excitation. The appropriate doping concentration of RE ions will not induce the complete scintillation quenching under X-ray excitation [33-35]. In addition, there are also some reports on Bi-based materials that show the absorption of *X*-ray, which are also typical lead-free perovskite materials.[36,37] Bi ions are

reported to improve the crystal perfection as well as the exciton localization for enhanced PLQY [38].

Herein, a lead-free $Yb^{3+}/Er^{3+}/Bi^{3+}$ co-doped double perovskite single crystal is developed, which features excellent multimodal and multicolor luminescence. Under the *X*-ray excitation, ultraviolet light and NIR laser (980 nm) irradiation, the warm yellow light, bright warm-white light, and green light are observed, respectively. Most importantly, the further experimental results also confirm the high stability against humidity, high temperature, high dose radiation of the as-synthesized material, opening the opportunities for flexible applications in *X*-ray detection and anti-counterfeiting as well as other daily applications.

Three RE-doped samples $Cs_2Ag_{0.6}Na_{0.4}InCl_6:Yb^{3+}/Er^{3+}/Bi^{3+}$ (**RE-1**), $Cs_2Ag_{0.6}Na_{0.4}InCl_6:Yb^{3+}/Er^{3+}$ (**RE-2**), $Cs_2AgInCl_6$: Yb^{3+}/Er^{3+} (**RE-3**) (top of Figure 1a) and one RE-free sample $Cs_2AgInCl_6$ (**RE-4**) were synthesized by a reported method with minor modifications.[28] Single crystal *X*-ray diffraction analysis results revealed that **RE-1** (*CSD No*. 1941823), **RE-2** (*CSD No*. 1976878) and **RE-3** (CSD No. 1976879) belong to the cubic space group $Fm\bar{3}m$ (225) and contains 8Cs, 4Ag/Na, 4In and 24Cl (bottom of **Figure 1**a). Yb^{3+}/Er^{3+}, Bi^{3+} and In^{3+} ions have similar ionic radii and valence states, and they occupy the same crystallographic site in the perovskite structure. These trivalent ions are surrounded by six Cl^- ions in an octahedral configuration. Ag^+ and Na^+ occupy the same site, which is also coordinated with six Cl^- ions, forming another octahedral coordination geometry. The $In^{3+}/RE^{3+}/Bi^{3+}$ and Ag^+/Na^+ based octahedrons are uniformly distributed in the perovskite structure, and Cs^+ is distributed between the sides of the two neighbouring octahedrons. The deviation of the different unit cell parameters among the structures of **RE-1**, **RE-2** and **RE-3** is less than 1% (Table S1), which are almost identical with the structures of $Cs_2AgInCl_6$ and $Cs_2NaInCl_6$, supporting the absence of secondary phases (Table S2).[28,39] Moreover, previous

works have systematically investigated the doping concentration of Na and Bi ions in $Cs_2AgInCl_6$, which indicates no obvious defects is formed at the doping concentration as **RE-1**[28,38]. Therefore, we confirm that all four compounds belong to the same crystal structures, in which **RE-1**, **RE-2** and **RE-3** maintained the pristine perfect structure of $Cs_2AgInCl_6$.

All of the compounds were characterized by the powder XRD (Figure 1b), and the results are in good agreement with the simulated diffraction pattern from the single crystal structure of **RE-1** (Figure S1). The diffraction peaks of the RE-doped samples shift to lower angles compared with the undoped one; according to Bragg Law, the doping of $Yb^{3+}/Er^{3+}/Bi^{3+}$ or Yb^{3+}/Er^{3+} ions lead to a slight expansion of the perovskite crystal cells (Figure 1c).[40] One of the reasons is that the RE ions have larger radii than indium ion. In addition, the different coordination affinity between Yb^{3+}/Er^{3+} and Cl^- ions in perovskite structure also leads to the slight lattice distortion.[41] The XRD patterns of **RE-1**, **RE-2,** and **RE-3** show similar changes. These results also confirmed that Yb^{3+}/Er^{3+} ions have been successfully doped into the lattice of perovskite materials.[24,40]

^{133}Cs and ^{115}In magic-angle spinning (MAS) solid-state NMR (SSNMR) spectra of **RE-1** and control sample ($Cs_2Ag_{0.6}Na_{0.4}InCl_6$:Bi) were recorded at 9.4 T to further analysis its fine structure. The doping of paramagnetic Yb^{3+} and Er^{3+} ions induces a shift of the ^{133}Cs peak at 103.3 ppm to 101.1 ppm as well as a significant broadening of this signal (the full-width-at-half-height increases from 173 to 300 Hz) (Figure 1d).[42,43] The shift of peak position is due to the delocalization of extra electron density of Yb^{3+} and Er^{3+} (spin I = 1/2 and 3/2) on Cs^+, i.e., the Fermi-contact interaction. The broadening of NMR peak corresponds to the accelerated transverse (T_2) relaxation of ^{133}Cs in the presence of adjacent paramagnetic Yb^{3+} and Er^{3+} ions, resulting from the strong dipolar coupling between unpaired electrons and ^{133}Cs nuclei (i.e., the pseudo-contact interaction). The longitudinal (T_1) relaxation constant also decreases from 218

seconds to 101 seconds in the Yb^{3+}/Er^{3+}-doped sample (Figure 1e).[44] The Cs−Cl−In/Bi environment is strongly affected by paramagnetic RE^{3+} ions (insert of Figure 1d). In the double perovskite structure, the very high spherical symmetry at In^{3+} enables the acquisition of high-resolution ^{115}In spectra (Figure 1f). Two ^{115}In peaks were observed at 51.9 ppm and 40.1 ppm in both samples, respectively. Similar to the Cs−Cl−Bi/In the environment, the more de-shielded peak at 51.9 ppm is assigned to the In−Cl−Ag environment whereas the 40.1 ppm peak is In−Cl−Na (Insert of Figure 1f).[45,46] The higher intensity of the peak at 40.1 ppm in the RE-free sample is also consistent with its higher concentration of Na. After the Yb^{3+}/Er^{3+}-doping, the relative intensity of the peak at 40.1 ppm decreased dramatically. The results from ^{133}Cs and ^{115}In SSNMR experiments further support that the Yb^{3+}/Er^{3+} ions have been successfully incorporated into the double perovskite lattice.[44] Furthermore, the Yb^{3+}/Er^{3+} ions are not distributed randomly in the sample: the effect of paramagnetic ions is distinct for Cs−Cl−In and Cs−Cl−Bi environments, as well as In−Cl−Ag and In−Cl−Na environments.[43,44] The Yb^{3+}/Er^{3+} ions are likely adjacent to the Cs−Cl−Bi and In−Cl−Na environments.

Since the absorption coefficient of the material is highly dependent on the specific element composition, we have further applied the scanning electron microscope energy dispersive spectrometer (SEM-EDS) and EDS-mapping to analyze the composition of each compound (Figure S2–S9). All the elements are evenly distributed in the images, with no element enrichment, which indicates that there was no phase separation in the as-prepared perovskite materials. According to the EDS spectra, the content and proportion of Cs^+, Ag^+, Na^+, In^{3+} and Cl^- are in good accordance with the expected values (Table S3). Owing to low doping contents of $Yb^{3+}/Er^{3+}/Bi^{3+}$ in **RE-1**, Yb^{3+}/Er^{3+} co-doped **RE-2** and **RE-3**, their contents were barely detectable by SEM-EDS. Therefore, the inductively coupled plasma mass spectroscopy (ICP-MS) was used to further determine the precise amounts of Yb^{3+}, Er^{3+}, Bi^{3+} in the as-prepared samples. The sum of these trivalent ions was calculated to determine the content proportion of

each specific ion. The content of each ion in the compounds is 99.38% for In^{3+}, 0.3% for Yb^{3+}, 0.08% for Er^{3+} and 0.24% for Bi^{3+} in **RE-1**; 99.51% for In^{3+}, 0.4% for Yb^{3+} and 0.09% for Er^{3+} in **RE-2**; 99.25% for In^{3+}, 0.6% for Yb^{3+} and 0.15% for Er^{3+} in **RE-3** (Table S4).

The sample **RE-1**, **RE-2**, **RE-3** and **RE-4** are pale yellow single crystals under natural light. As shown in **Figure 2**a-b, the samples have no emission with the light off or in the darkroom. Under *X*-ray excitation, only **RE-1** emits the yellow-white light. In comparison, under the excitation of the ultraviolet lamp (365 nm or 254 nm), **RE-1** and **RE-2** both emit warm white light, in which the luminescence intensity of **RE-1** is higher than that of **RE-2**. Similar to X-ray excitation, both **RE-3** and **RE-4** have no emission under an ultraviolet lamp. Under NIR laser irradiation, **RE-1**, **RE-2** and **RE-3** emit green light. The intensity of green light for **RE-1** is greater than that of **RE-2**, and the weakest for **RE-3**. **RE-4** has no luminescence emission under 980 nm laser excitation since it is RE-free. More importantly, **RE-1** and **RE-2** can emit both DS luminescence and UC phosphorescence under the simultaneous excitations of NIR laser and ultraviolet lamp. The emission of the samples can be seen from the supplementary Video S1. **RE-1** does not emit light without any excitation. When it is irradiated by NIR laser and ultraviolet light at the same time, it can emit green light and warm white light. And it emits only green light under NIR radiation, warm white light under the sole excitation of the ultraviolet lamp. The video of **RE-1** was also recorded in the XRD test room: when *X*-ray was off, the sample did not emit light; when *X*-ray was on, the sample emitted warm yellow light (Video S2).

To further investigate the luminescence properties of **RE-1**, the multimodal luminescence spectra of **RE-1** were shown in Figure 2c. The optimized ratio of Yb^{3+}/Er^{3+} has been confirmed based on experiments and previous works (Figure S10)[47]. Under various stimuli, **RE-1** can emit different luminescence. As shown in Figure 2d, the DS PL spectra were measured under

UV light excitation (λ_{ex} = 365 nm). The samples show wide emission spectra from 400 nm to 710 nm, with the emission peak ranging in 553 – 585 nm. The luminescence decay curves at 560 nm of the four samples indicated that **RE-1** has a longer luminescent decay lifetime (Figure 2e). The excitation spectra of these four samples revealed that they have different excitation peaks (Figure S11): **RE-1** has an excitation peak at 365 nm, and the excitation band ranges roughly from 345 nm to 395 nm; **RE-2** has three excitation peaks at 308, 356 and 386 nm, and **RE-3** and **RE-4** both have a peak at 364 nm, which indicated that **RE-1** has a wider and more sensitive response capacity to UV light. Under the excitation of NIR laser (980 nm), sensitizer ions Yb^{3+} absorb this NIR energy and transfer to the luminescence center ion Er^{3+} in the energy level of $^4I_{13/2}$, $^4I_{11/2}$, $^4F_{9/2}$ and $^4F_{7/2}$, and the energy transfer to the energy level of $^4I_{15/2}$ to emit UC PL in **RE-1**, **RE-2** and **RE-3**. This energy mechanism is different with previous work of RE-doped double perovskite, where Ho3+ ions absorb energy from the host material [29]. The emission spectra of all the samples under *X*-ray excitation were shown in Figure 2f, all four samples emit broad emission bands from 450 nm to 850 nm, the peak of the spectra are all about 627 nm, in which **RE-1** has stronger emission. Understanding the mechanism of the Jahn-Teller of octahedral distortion in the double perovskite is critical for the optimization of the luminescence properties. The varied stoke shift of the self-trapped excitons (STE) emission derives from the different deformation levels of the Jahn-Teller effect induced by the UV light and high energy X-ray excitation, which further affects the deformation energy and photoluminescence energy [48]. The DS PL and XEL emission spectra show that doping of Bi ions into the material improved the ability of the material to absorb high-energy excitation, and further enhanced its luminescence properties. Until recently, RE doped double perovskite materials are reported with UC phenomenon[49,50]. In our work, it is noted that the Yb^{3+}/Er^{3+} co-doped samples **RE-1**, **RE-2** and **RE-3** emit UC PL of Yb^{3+}/Er^{3+} ions (Figure 2g). Under the excitation of NIR laser (980 nm), the three Yb^{3+}/Er^{3+} co-doped samples all emit three characteristic peaks of Er^{3+} at 527 nm, 555 nm and 660 nm, and the corresponding energy level

transitions are $^2H_{11/2}\rightarrow{}^4I_{15/2}$, $^4S_{3/2}\rightarrow{}^4I_{15/2}$ and $^4F_{9/2}\rightarrow{}^4I_{15/2}$, respectively. Although the RE doped luminescence properties of $Cs_2Ag_{1-x}Na_xInCl_6$ has been reported in previous works by Tang *et al.*, the upconversion properties are usually not involved [51]. This is attributed to the different energy transfer mechanism, where the Yb ions are able to directly absorb the excitation energy rather than indirectly absorbing from the host. The luminescence decay curves of **RE-1**, **RE-2** and **RE-3** fitted luminescence lifetimes show that **RE-1** has the longest luminescence lifetime up to 2 ms (Figure 2h). Since **RE-1** has displayed better multimodal luminescence performances than other samples, we focus on its excellent properties and versatile applications. With the increase of laser (980 nm) power, the UC PL intensity of the **RE-1** increases gradually (Figure S12a). In order to better understand the UC mechanism of the materials, the curves of the characteristic emission peak areas *vs* power densities of Er^{3+} ion at 527 nm, 555 nm and 660 nm were given in the inset.[52] The fitting results show that the slopes of the three lines are about 2.2, 2.0 and 2.3, respectively. The results show that these three kinds of emission follow the two-photon energy conversion mechanism. The UC diagram of the energy transfer process between the sensitizer ion Yb^{3+} and the activator ion Er^{3+} is shown in Figure S12b.[13,18,53] The DS luminescence process of **RE-1** has been reported in the literature, which belongs to exciton self-trap emission.[28] The lattice atoms in **RE-1** absorbed *X*-ray and ionized to form highly active electrons and holes, then the outside atoms were thermalized and secondary low-energy electrons and holes were produced.[37] Then the low-energy particles formed excitons, which were confined into the lattice of $AgCl_6$ and formed the XEL emission center.[25,54] Finally, **RE-1** emits a wide and strong XEL band. A small amount of Bi^{3+} doped into **RE-1** structure absorbs the high energy from *X*-ray, which enhances the structure perfection, promotes the exciton localization, and further improves the XEL performance as well as the photoluminescence quantum yield (PLQY).[17,28,36,55]

Meanwhile, in order to further study the influence of defect concentrations on the luminescence performance in the same material, we apply varied external pressure on the material systems to create defects in **RE-1**. The up-conversion photoluminescence (UC PL) spectra of RE-1 under different pressure was shown in Figure S13. As the external pressure increases, the UC PL emission intensity gradually decreases. When the applied pressure reaches 17.04 GPa, the UC PL emission of **RE-1** nearly disappears. These results confirm that the defects in the materials induced by the external high pressure are able to significantly quench the UC PL. This is similar to the results reported in the recently published work [47]. After removing the external pressure, the UC PL of **RE-1** cannot fully restore to the original level, indicating the irreversible distortion of the structure with defects. And the irreversible formation of defects has hindered the luminescent properties of **RE-1**. Therefore, the defect passivation by the introduction of Yb^{3+}/Er^{3+}/Bi^{3+} also contributes to the significantly improved luminescence performances of **RE-1**.

The stability of **RE-1** was characterized by temperature-dependent XRD (**Figure 3**a). **RE-1** shown inevitable crystal expansion at high temperature, the diffraction peak blue shifted along as the diffraction angle decreased slightly. No other notable changes in the diffraction patterns were detected even after cooling to room temperature. **RE-2** also shows the same high-temperature stability (Figure S14). The thermal stability of **RE-1** was also characterized by thermogravimetric (TG) analysis (Figure 3b), the TG curve shows that **RE-1** is highly stable below 500 ºC, and there is no observable weight loss. When the temperature rises from ~520 ºC to ~710 ºC, the weight loss about 33% of the samples comes from the salt ($InCl_3$ and $BiCl_3$) with a low boiling point. As the temperature continues to rise, the azeotropy of the residual molten salts induces further weightlessness. The TG curves of **RE-2** and **RE-3** are similar to that of **RE-1** (Figure S15). These results also show consistent conclusion that the introduction of Na will not affect the stability at the appropriate concentration, which increases the

decomposition temperature and emission stability [28]. Therefore, those samples have excellent thermal stability until 500 ºC, extending their application durability in a much harsher environment.

Compared with the CsI:Tl, RE-1 shows idea XEL performance and responds to the light with a wider range of wavelength, and its XEL emission intensity up to a quarter of CsI:Tl (Figure S16). In order to assess the luminescence stability of **RE-1** against *X*-ray with high radiation dosage, we recorded its XEL spectra after exposure under continuous radiation conditions (Figure 3c, Figure S17). When the radiation reached to 13 Gy, the retained XEL intensity of **RE-1** (70%) is lower than that of CsI:Tl (97%); when the radiation increased to 29 Gy, the XEL intensity of **RE-1** (60%) is stronger than that of CsI:Tl (50%); when the radiation continued to increase to 53 Gy, the XEL intensity of **RE-1** retained 49%, whereas 28% was retained for CsI:Tl (Table S5).[56] The results show that **RE-1** has higher stability and an excellent XEL property against radiation than that of CsI:Tl even under high-dosage *X*-ray radiation. Stability test against humidity shows that the XEL intensity of **RE-1** and CsI:Tl decrease gradually with the increase of the relative humidity (Figure 3d, Figure S18). Nonetheless, compared with the commercial CsI:Tl scintillator, **RE-1** still has significantly higher stability against humidity.[56] CsI:Tl was kept in the environment of 40% relative humidity (RH), 60% RH and 95% RH for 30 mins, its XEL intensity remained at about 31%, 28% and 5%. While, **RE-1** remained the higher XEL emission intensity of 82%, 57% and 27% in more humid conditions of 45% RH, 65% RH and 95% RH kept for a longer process of 90 mins. (Table S6). Therefore, **RE-1** present more excellent stability against the humidity than CsI:Tl, and further proved that **RE-1** has appreciable application prospect, which could serve as an excellent scintillator to fabricate high performance and long-period devices for radiation detection.[17,56]

The luminescence spectra of **RE-1** under different powers of the *X*-ray anode tube is shown in Figure 3e. With the voltage kept constant (40 kV), the current increased from 15 mA to 40 mA, the XEL spectra show that the emission intensity of the sample increased gradually. The XEL spectra of the intensity at 627 nm ($\boldsymbol{I}_{627\ nm}$) *vs* the *X*-ray dosage rate gave a good linear fitting (Figure 3f, Figure S19). The limit of detection (LOD) was calculated according to the equation of LOD = 3 *SD*/*K* gave a lower value of 8.2 nGy/s,[57] where *SD* (0.0675) is the instrument standard deviation and *K* (24.58) is the slope of the calibration curve in Figure 3f. The result indicated that this material is suitable for *X*-ray detection. The absorption coefficient of **RE-1** particularly similar to that of the commercial CsI:Tl (Figure 3g). However, the density of **RE-1** (3.99 g/cm^3) is smaller than CsI:Tl (4.51 g/cm^3), which indicates that **RE-1** has the ideal ability to absorb the radioactive substance. In addition, **RE-1** is also able to serve as colorless pigment for security printing. As shown in Figure 3h, the patterns printed by invisible printing is colorless under visible light, and the patterns and the paper show the same color tone, which cannot be directly identified by naked eyes. By contrast, under the ultraviolet lamp (365 nm) irradiation (Figure 3i), it can be seen as the patterns presented in the paper clearly. Moreover, the prepared labels still reserve the printed anti-counterfeiting patterns after being stored in the atmosphere for 3 months (Figure S20). This shows that excellent information storage and readout capability of the anti-counterfeiting label prepared by **RE-1**. Therefore, the utilization of **RE-1** in the field of security printing for anti-counterfeiting labels or confidential documents is highly promising in the future.

We have investigated the $Cs_2AgInCl_6$ regarding the projected density of states (PDOSs) and lattice structure. $Cs_2AgInCl_6$ is constructed by two octahedrons [$AgCl_6$] and [$InCl_6$], which shows uniform Ag-Cl and In-Cl bond length of 2.751 Å and 2.581 Å, respectively. Notably, the p-orbitals dominates the PDOSs near the Fermi level (E_F), which consists of the main contribution from Cl-2*p*. The d-orbitals from Ag occupy a slightly lower position than the p-

orbitals. The bonding and anti-bonding of $Cs_2AgInCl_6$ show that bonding is controlled by Cl-2*p* orbitals while the anti-bonding display mixing contribution of *s,p* orbitals from Cs and In (**Figure 4**a). With the introduction of Na in Ag sites, the corresponding d orbital contributions become lower while the contribution of the *s,p* orbitals slightly increases. Accordingly, the anti-bonding sites have been concentrated on In sites. Due to the larger size of Na^+ (1.15 Å) than Ag^+ (1.02 Å), the structure of $[AgCl_6]$ octahedron shows a slight expansion in the axial and planar directions. The radius of the $[NaCl_6]$ and $[AgCl_6]$ is 2.78 and 2.69 Å, respectively. Meanwhile, we notice that the introduction of Na does not contribute to the conduction band minimum (CBM) or the valence-band maximum (VBM), supporting the main role of Na ions is to isolate the $[AgCl_6]$ octahedron and confine the spatial distribution of single exciting states (Figure 4b) [28]. For the Yb dopant, 4*f* bands mainly locate on E_F, supporting an electron transfer center for luminescence. The bonding orbitals show a mixing contribution from Ag-4*d*, Cl-2*p*, and Yb-4*f* orbitals while a small part of anti-bonding orbitals locates on Cl-2*p* rather than the pure In-5s, 5p. Although Yb shows the larger atomic radius than the In, $[AgCl_6]$ becomes compression in all directions (Figure 4c). The bonding orbital components include Cl-2*p*, Ag-4*d*, and Bi-6*p* orbitals. PDOSs show the increased contribution by p-orbitals below the conduction band, which is induced by the $[BiCl_6]$ states, indicating the improved luminescence performance based on the trapped emission between states localized in the $[BiCl_6]$ and $[AgCl_6]$ octahedron[38]. Based on the PDOSs results, the local electronic structure reveals a high electronic sensitivity to the dopants (Figure 4d).

Most importantly, the introduction of Bi leads to the strong Jahn-Teller effect within the d^9 electronic configuration of Ag by the large 6s orbitals, which distorted the $[AgCl_6]$ octahedron and breaks the inversion-symmetry-induced parity-forbidden transition for luminescence. The distortion level of the octahedron is becoming stronger from $Cs_2AgInCl_6$ to $Cs_2Ag_{0.6}Na_{0.4}InCl_6$:Yb/Bi (Figure 4e). The introduction of Bi interrupts the local crystal field,

which results in a contrast Jahn-Teller distortion, in which the [$AgCl_6$] and [$InCl_6$] octahedron undergo the tetragonal compression and elongation, respectively. The s-s repulsive force between the Bi and Yb suppresses the closed-shell effect in Yb, which activates the remarkable luminescence (Figure 4f). Within the introduction of the Na in the system, we do not observe the significant change in both intensity and peak positions in simulated absorption spectra. Bi dopants significantly activate the photoluminescence at a lower frequency, which is supportive evidence of the enhanced X-ray excitation luminescence in Yb/Er-doped $Cs_2Ag_{0.6}Na_{0.4}In(Bi)Cl_6$ (Figure 4g). The dramatic boost in dielectric function by Bi-dopant is noted, which strongly supports the exceptional X-ray excitation luminescence. The detailed explanation of the mechanism has been supplied in supporting information of Figure S20, which is correlated with the structural disorder levels. The similar dielectric function of $Cs_2AgInCl_6$, $Cs_2Ag_{0.6}Na_{0.4}InCl_6$, $Cs_2Ag_{0.6}Na_{0.4}InCl_6$:Yb and $Cs_2Ag_{0.6}Na_{0.4}InCl_6$:Yb/Bi are also consistent with the subtle change in both X-ray excitation experiments (Figure 4h). The formation of defects in different samples is also investigated, in which the formation of anion vacancy is much easier than the cation vacancies. The introduction of $Yb^{3+}/Er^{3+}/Bi^{3+}$doping has resulted in the highly difficult for the formation of both cation and anion vacancies in the materials, which is fully consistent with previous work[28], confirming the high stability of the doped samples. Although the Ag and Cl vacancies show much lower energy cost than In and Cs vacancies, the formation of defect still shows over 1 eV energy barrier height, supporting the defect passivation, which is consistent with the experimental results of defect formation (Figure 4i). In addition, we also conduct the numerical simulation of the dynamic PL spectra of RE-1, RE-2, and RE-3 for comparison, in which the stronger Jahn Teller effect induces the stronger UC PL and longer decay time (Figure S21-S22).

In summary, the $Yb^{3+}/Er^{3+}/Bi^{3+}$ tri-doping double perovskite has been synthesized successfully with the multimodal luminescent performance. The incorporation of rare-earth ions and Bi^{3+}

ions successfully activated the concurrent excellent UC PL, DS PL, and XEL performance for the first time. Moreover, the superior stability against the harsh environment has also been achieved including the thermal stability up to 400 °C, the humidity, and high-dosage radiation resistance. Featuring such capabilities, the material shows high X-ray sensitivity with a low LOD of 8.2 nGy/s, endowing them the potential for practical and robust anti-counterfeiting printing. Moreover, DFT calculations also confirm that the introduction of dopants not only passivate the defects but also significantly improve the luminescence performance due to the MRO and Jahn-Teller effect. Therefore, this toxic-element-free material has paved a new direction for designing and fabricating environment-friendly multimodal luminescence materials for realizing high-level anticounterfeiting techniques, which is also beneficial for the developments of multifunctional luminescent materials in the future.

Supporting Information
Supporting Information is available from the Wiley Online Library or from the author.

Acknowledgements
We gratefully acknowledge the support from the China National Funds for Excellent Young Scientists (Grant No.: 21522106) and National Natural Science Foundation of China (Grant No.:21971117; 21771156), 111 Project (B18030) from China, and the Open Funds (RERU2019001) of the State Key Laboratory of Rare Earth Resource Utilization, the Functional Research Funds for the Central Universities, Nankai University (ZB19500202), the Shenzhen Fundamental Research Project (Grant No.: JCYJ20170818100717134) and the Early Career Scheme (ECS) fund (Grant No.: PolyU 253026/16P) from the Research Grant Council (RGC) in Hong Kong. We gratefully acknowledge the support of the University Research Facility on Chemical and Environmental Analysis (UCEA) of PolyU for the Solid-state NMR testing and data analysis. We also greatly thank Mingxing Chen at Analytical Instrumentation Center of Peking University, for his support in spectral measurement.

Received: ((will be filled in by the editorial staff))
Revised: ((will be filled in by the editorial staff))
Published online: ((will be filled in by the editorial staff))

References

[1] Zang, X.; Dong, F.; Yue, F.; Zhang, C.; Xu, L.; Song, Z.; Chen, M.; Chen, P. Y.; Buller, G. S.; Zhu, Y.et al. *Adv. Mater.* **2018,** *30*, e1707499.
[2] Bae, H. J.; Bae, S.; Park, C.; Han, S.; Kim, J.; Kim, L. N.; Kim, K.; Song, S. H.; Park, W.; Kwon, S. *Adv. Mater.* **2015,** *27*, 2083.

[3] Jiang, K.; Zhang, L.; Lu, J.; Xu, C.; Cai, C.; Lin, H. *Angew. Chem. Int. Ed. Engl.* **2016,** *55*, 7231.
[4] Andres, J.; Hersch, R. D.; Moser, J.-E.; Chauvin, A.-S. *Adv. Funct. Mater.* **2014,** *24*, 5029.
[5] Li, X.; Xie, Y.; Song, B.; Zhang, H. L.; Chen, H.; Cai, H.; Liu, W.; Tang, Y. *Angew. Chem. Int. Ed. Engl.* **2017,** *56*, 2689.
[6] Zhou, B.; Yan, L.; Tao, L.; Song, N.; Wu, M.; Wang, T.; Zhang, Q. *Adv Sci (Weinh)* **2018,** *5*, 1700667.
[7] Xu, J.; Zhang, B.; Jia, L.; Fan, Y.; Chen, R.; Zhu, T.; Liu, B. *ACS Appl Mater Interfaces* **2019,** *11*, 35294.
[8] Zhou, D.; Liu, D.; Xu, W.; Chen, X.; Yin, Z.; Bai, X.; Dong, B.; Xu, L.; Song, H. *Chem. Mater.* **2017,** *29*, 6799.
[9] Ren, Y.; Yang, Z.; Li, M.; Ruan, J.; Zhao, J.; Qiu, J.; Song, Z.; Zhou, D. *Advanced Optical Materials* **2019,** *7*.
[10] Wu, C.; Zeng, S.; Wang, Z.; Wang, F.; Zhou, H.; Zhang, J.; Ci, Z.; Sun, L. *Adv. Funct. Mater.* **2018,** *28*.
[11] Xu, L.; Chen, J.; Song, J.; Li, J.; Xue, J.; Dong, Y.; Cai, B.; Shan, Q.; Han, B.; Zeng, H. *ACS Appl Mater Interfaces* **2017,** *9*, 26556.
[12] Liu, X.; Yan, C. H.; Capobianco, J. A. *Chem. Soc. Rev.* **2015,** *44*, 1299.
[13] Dong, H.; Sun, L. D.; Yan, C. H. *Chem. Soc. Rev.* **2015,** *44*, 1608.
[14] Chen, L.; Yan, C.; Pan, M.; Wang, H.-P.; Fan, Y.-N.; Su, C.-Y. *Eur. J. Inorg. Chem.* **2016,** *2016*, 2676.
[15] Tan, Z.; Li, J.; Zhang, C.; Li, Z.; Hu, Q.; Xiao, Z.; Kamiya, T.; Hosono, H.; Niu, G.; Lifshitz, E.et al. *Adv. Funct. Mater.* **2018,** *28*, 1801131.
[16] Sun, X.-Y.; Yu, X.-G.; Jiang, D.-G.; Wang, W.-F.; Li, Y.-N.; Chen, Z.-Q.; Zhou, Y.-Z.; Yang, Q.-M.; Kang, Z. *J. Appl. Phys.* **2016,** *119*, 233103.
[17] Wang, Y.; Wang, Y.; Dai, X.; Liu, W.; Yin, X.; Chen, L.; Zhai, F.; Diwu, J.; Zhang, C.; Zhou, R.et al. *Inorg. Chem.* **2019,** *58*, 2807.
[18] Huang, B.; Sun, M.; Dougherty, A. W.; Dong, H.; Xu, Y. J.; Sun, L. D.; Yan, C. H. *Nanoscale* **2017,** *9*, 18490.
[19] Soo, Y. L.; Huang, S. W.; Kao, Y. H.; Chhabra, V.; Kulkarni, B.; Veliadis, J. V. D.; Bhargava, R. N. *Appl. Phy. Let.* **1999,** *75*, 2464.
[20] Zuniga, J. P.; Gupta, S. K.; Pokhrel, M.; Mao, Y. *New J. Chem.* **2018,** *42*, 9381.
[21] Kumar, K. N.; Vijayalakshmi, L.; Choi, J. *Inorg. Chem.* **2019,** *58*, 2001.
[22] Wu, K.; Zhang, J.; Fan, S.; Li, J.; Zhang, C.; Qiao, K.; Qian, L.; Han, J.; Tang, J.; Wang, S. *Chem. Commun. (Cambridge, U. K.)* **2015,** *51*, 141.
[23] Li, Y.; Di, Z.; Gao, J.; Cheng, P.; Di, C.; Zhang, G.; Liu, B.; Shi, X.; Sun, L. D.; Li, L.et al. *J. Am. Chem. Soc.* **2017,** *139*, 13804.
[24] Zhang, X.; Zhang, Y.; Zhang, X.; Yin, W.; Wang, Y.; Wang, H.; Lu, M.; Li, Z.; Gu, Z.; Yu, W. W. *J Mater Chem C Mater* **2018,** *6*, 10101.
[25] Chen, Q.; Wu, J.; Ou, X.; Huang, B.; Almutlaq, J.; Zhumekenov, A. A.; Guan, X.; Han, S.; Liang, L.; Yi, Z.et al. *Nature* **2018,** *561*, 88.
[26] Xiao, Z.; Song, Z.; Yan, Y. *Adv. Mater.* **2019,** *31*, e1803792.
[27] Yang, B.; Hong, F.; Chen, J.; Tang, Y.; Yang, L.; Sang, Y.; Xia, X.; Guo, J.; He, H.; Yang, S.et al. *Angew. Chem. Int. Ed. Engl.* **2019,** *58*, 2278.
[28] Luo, J.; Wang, X.; Li, S.; Liu, J.; Guo, Y.; Niu, G.; Yao, L.; Fu, Y.; Gao, L.; Dong, Q.et al. *Nature* **2018,** *563*, 541.
[29] Zhu, W.; Ma, W.; Su, Y.; Chen, Z.; Chen, X.; Ma, Y.; Bai, L.; Xiao, W.; Liu, T.; Zhu, H.et al. *Light Sci Appl* **2020,** *9*, 112.
[30] Zhou, J.; Xia, Z.; Molokeev, M. S.; Zhang, X.; Peng, D.; Liu, Q. *J. Mater. Chem. A* **2017,** *5*, 15031.

[31] Askerka, M.; Li, Z.; Lempen, M.; Liu, Y.; Johnston, A.; Saidaminov, M. I.; Zajacz, Z.; Sargent, E. H. *J. Am. Chem. Soc.* **2019,** *141*, 3682.
[32] Igbari, F.; Wang, Z. K.; Liao, L. S. *Adv. Energy Mater.* **2019,** *9*, 1803150.
[33] Wojtowicz, A. J. *Nuclear Instruments and Methods in Physics Research Section A: Accelerators, Spectrometers, Detectors and Associated Equipment* **2002,** *486*, 201.
[34] Sun, C.; Pratx, G.; Carpenter, C. M.; Liu, H.; Cheng, Z.; Gambhir, S. S.; Xing, L. *Adv. Mater.* **2011,** *23*, H195.
[35] Stanton, I. N.; Ayres, J. A.; Therien, M. J. *Dalton Trans* **2012,** *41*, 11576.
[36] Pan, D.-J.; Yang, Y.-L.; Yang, X.-C.; Xu, T.; Cui, Y.-Y.; Sun, X.-Y.; Feng, H.; Liu, L.; Shen, Y.-F.; Zhao, J.-T.et al. *J. Alloys Compd.* **2018,** *742*, 1037.
[37] Steele, J. A.; Pan, W.; Martin, C.; Keshavarz, M.; Debroye, E.; Yuan, H.; Banerjee, S.; Fron, E.; Jonckheere, D.; Kim, C. W.et al. *Adv. Mater.* **2018,** *30*, e1804450.
[38] Locardi, F.; Sartori, E.; Buha, J.; Zito, J.; Prato, M.; Pinchetti, V.; Zaffalon, M. L.; Ferretti, M.; Brovelli, S.; Infante, I.et al. *ACS Energy Letters* **2019,** *4*, 1976.
[39] Luo, J. J.; Li, S. R.; Wu, H. D.; Zhou, Y.; Li, Y.; Liu, J.; Li, J. H.; Li, K. H.; Yi, F.; Niu, G. D.et al. *Acs Photonics* **2018,** *5*, 398.
[40] Lv, X.; Wu, J.; Zhu, J.; Xiao, D.; Zhang, X. x. *J. Am. Ceram. Soc.* **2018,** *101*, 4084.
[41] Zhou, D.; Liu, D.; Pan, G.; Chen, X.; Li, D.; Xu, W.; Bai, X.; Song, H. *Adv. Mater.* **2017,** *29*, 1704149.
[42] Ohkubo, T.; Okamoto, T.; Kawamura, K.; Guegan, R.; Deguchi, K.; Ohki, S.; Shimizu, T.; Tachi, Y.; Iwadate, Y. *J. Phys. Chem. A* **2018,** *122*, 9326.
[43] Kubicki, D. J.; Prochowicz, D.; Hofstetter, A.; Zakeeruddin, S. M.; Gratzel, M.; Emsley, L. *J. Am. Chem. Soc.* **2017,** *139*, 14173.
[44] Xiang, W.; Wang, Z.; Kubicki, D. J.; Tress, W.; Luo, J.; Prochowicz, D.; Akin, S.; Emsley, L.; Zhou, J.; Dietler, G.et al. *Joule* **2019,** *3*, 205.
[45] Yamada, K.; Mohara, H.; Kubo, T.; Imanaka, T.; Iwaki, K.; Ohki, H.; Okuda, T. *Z. Naturforsch. A* **2002,** *57*, 375.
[46] Yamada, K.; Kumano, K.; Okuda, T. *Solid State Ionics* **2005,** *176*, 823.
[47] Mai, H.-X.; Zhang, Y.-W.; Sun, L.-D.; Yan, C.-H. *The Journal of Physical Chemistry C* **2007,** *111*, 13721.
[48] Li, S.; Luo, J.; Liu, J.; Tang, J. *J Phys Chem Lett* **2019,** *10*, 1999.
[49] Wu, Y.; Lai, F.; Liu, B.; Li, Z.; Liang, T.; Qiang, Y.; Huang, J.; Ye, X.; You, W. *Journal of Rare Earths* **2020,** *38*, 130.
[50] Kumar, K. N.; Vijayalakshmi, L.; Choi, J. *Inorg. Chem.* **2019,** *58*, 2001.
[51] Li, S.; Hu, Q.; Luo, J.; Jin, T.; Liu, J.; Li, J.; Tan, Z.; Han, Y.; Zheng, Z.; Zhai, T.et al. *Advanced Optical Materials* **2019,** *7*.
[52] Dong, H.; Sun, L. D.; Wang, Y. F.; Ke, J.; Si, R.; Xiao, J. W.; Lyu, G. M.; Shi, S.; Yan, C. H. *J. Am. Chem. Soc.* **2015,** *137*, 6569.
[53] Dong, H.; Sun, L. D.; Feng, W.; Gu, Y.; Li, F.; Yan, C. H. *ACS Nano* **2017,** *11*, 3289.
[54] Yuan, W.; Niu, G.; Xian, Y.; Wu, H.; Wang, H.; Yin, H.; Liu, P.; Li, W.; Fan, J. *Adv. Funct. Mater.* **2019,** *29*, 1900234.
[55] González Mancebo, D.; Becerro, A. I.; Corral, A.; Moros, M.; Balcerzyk, M.; Fuente, J. M. d. l.; Ocaña, M. *ACS Omega* **2019,** *4*, 765.
[56] Wang, Y.; Yin, X.; Liu, W.; Xie, J.; Chen, J.; Silver, M. A.; Sheng, D.; Chen, L.; Diwu, J.; Liu, N.et al. *Angew. Chem. Int. Ed. Engl.* **2018,** *57*, 7883.
[57] Zhang, Y.; Liu, Z.; Yang, K.; Zhang, Y.; Xu, Y.; Li, H.; Wang, C.; Lu, A.; Sun, S. *Sci. Rep.* **2015,** *5*, 8172.

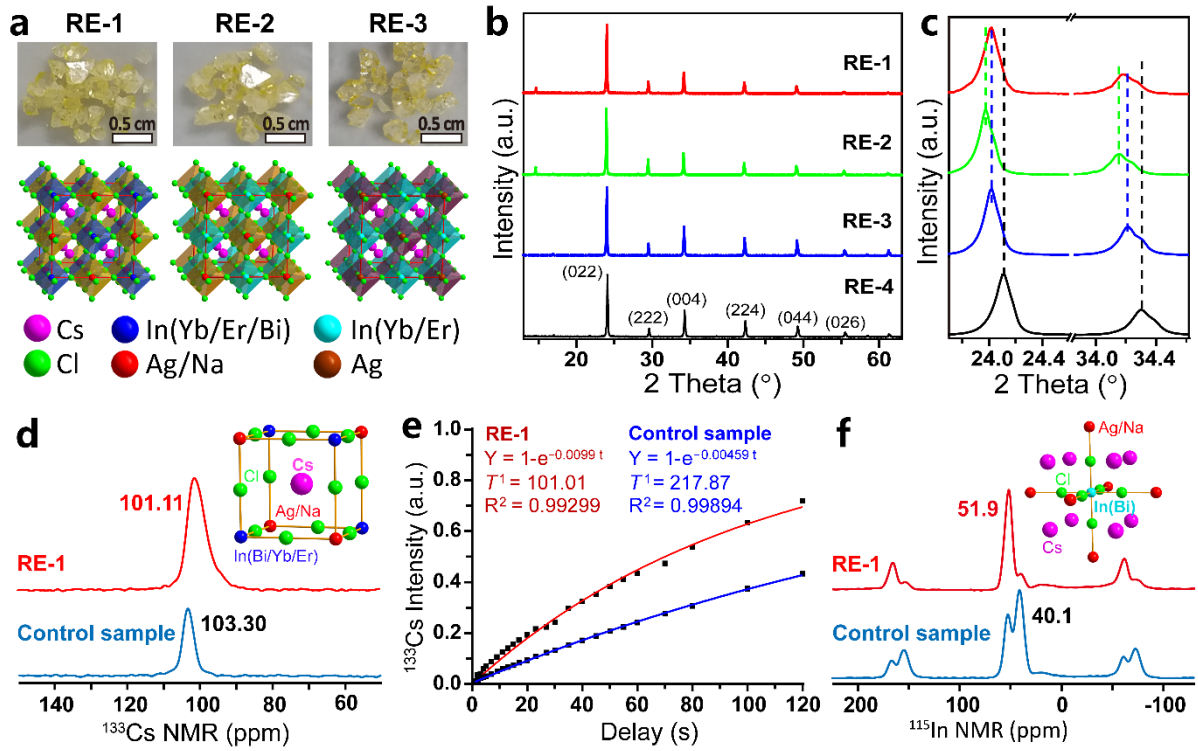

Figure 1. (a) The photographs and single crystal structures of RE-1, RE-2 and RE-3. (b) The XRD patterns of Yb^{3+}/Er^{3+} co-doped double perovskite, (c) the magnified XRD patterns in the region of 23°–43° in (b). The SSNMR spectra of RE-1 and control sample ($Cs_2Ag_{0.6}Na_{0.4}InCl_6$:Bi), (d) ^{133}Cs NMR spectra, (e) the ^{133}Cs spin-lattice relaxation times (T_1). (f) ^{115}In NMR spectra of the two samples. The inset in (e) and (f) show the coordination environments of Cs and In atoms.

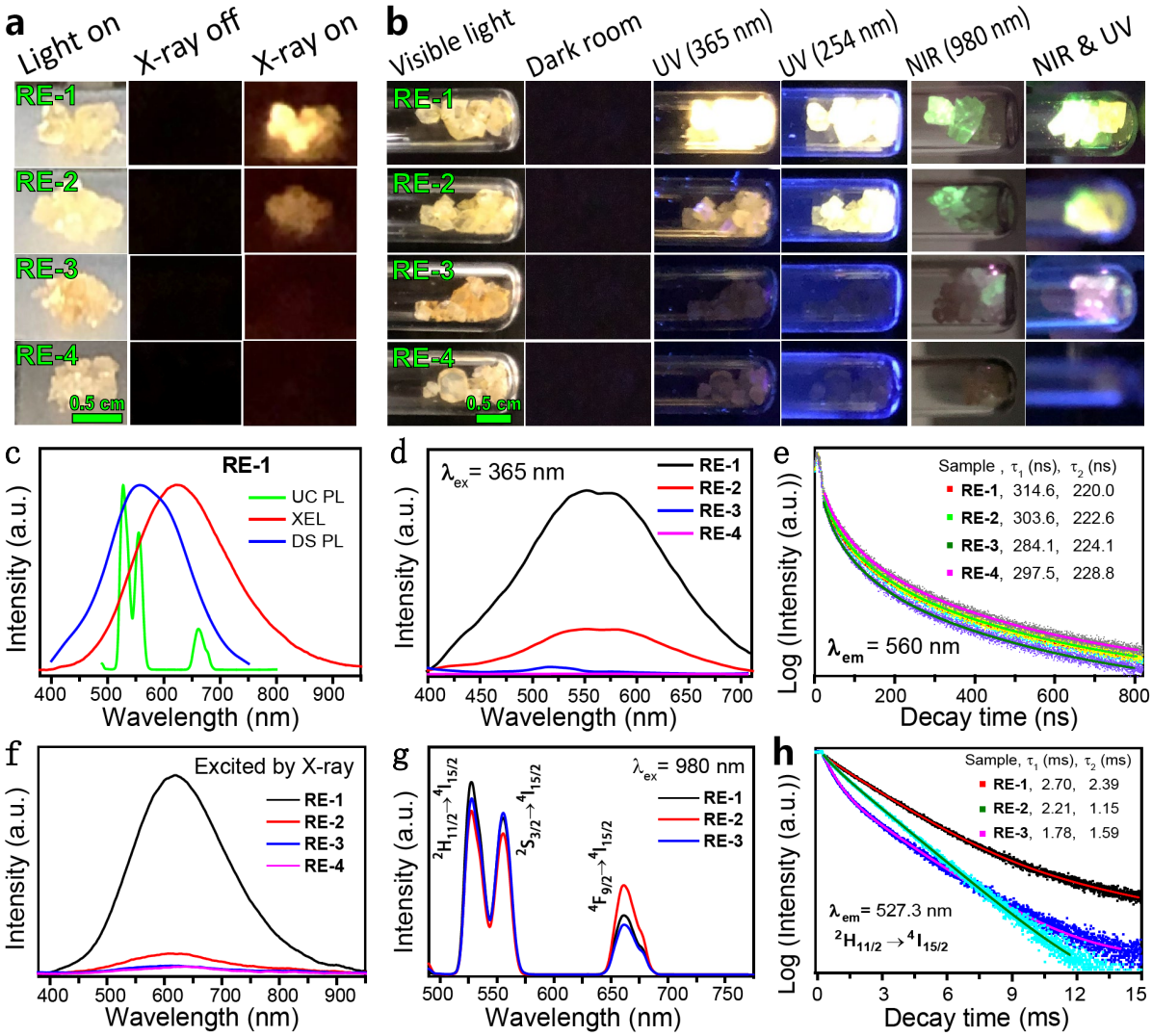

Figure 2. The photographs of **RE-1**, **RE-2**, **RE-3** and **RE-4** under different stimuli. (a) The samples put on the sample stage of an *X*-ray diffractometer and (b) the samples put in glass tubes. (c) The XEL (excited by X-ray), DS PL (λ_{ex} = 365 nm) and UC PL (λ_{ex} = 980 nm) spectra of **RE-1**. (d) DS PL spectra and (e) the DS PL decay curves of **RE-1**, **RE-2**, **RE-3**, **RE-4** emission at 560 nm (λ_{ex} = 365 nm). (f) XEL spectra of the **RE-1**, **RE-2**, **RE-3** and **RE-4**. (g) The UC PL spectra and (h) UC PL decay curves of **RE-1**, **RE-2** and **RE-3**.

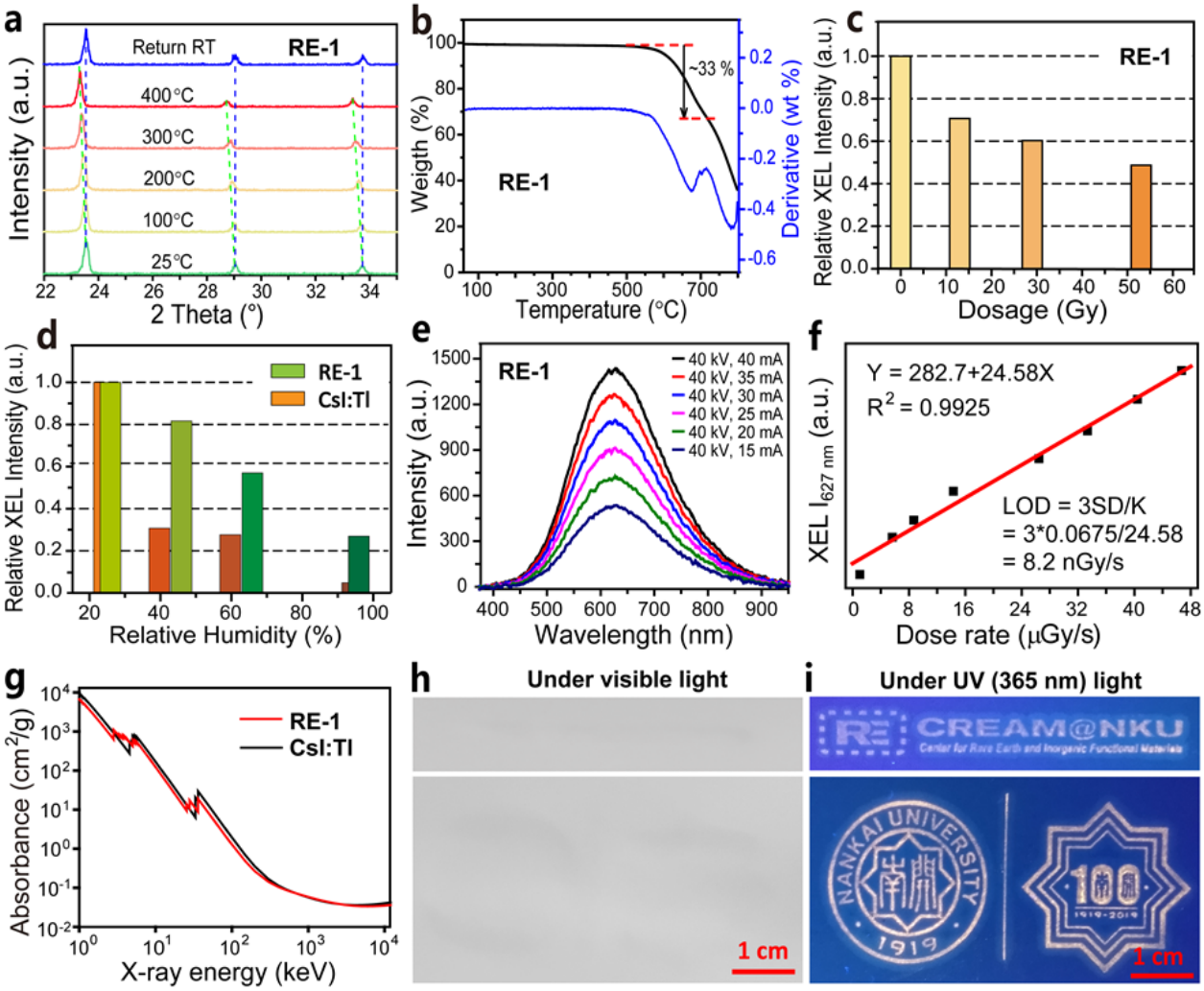

Figure 3. (a) The temperature-dependent XRD patterns of **RE-1**. (b) Thermogravimetric analysis graphs of **RE-1.** The relative XEL intensity at 627 nm of (c) **RE-1** after exposure under different doses *X*-ray and (d) **RE-1** and CsI:Tl being treated under different humidity conditions. (e) The XEL spectra of **RE-1** upon the increasing power of *X*-ray cathode tube. (f) The XEL intensity of **RE-1** at 627 nm varies with different *X*-ray dosage. (g) Simulated X-ray absorption spectra of **RE-1** and CsI:Tl. (h-i) The digital photographs of a luminescent badge with the Logos of '*Center for Rare Earth and Inorganic Functional Materials*' and *'NANKAI UNIVERSITY*' were stamped by the signets under visible light and UV light (365 nm).

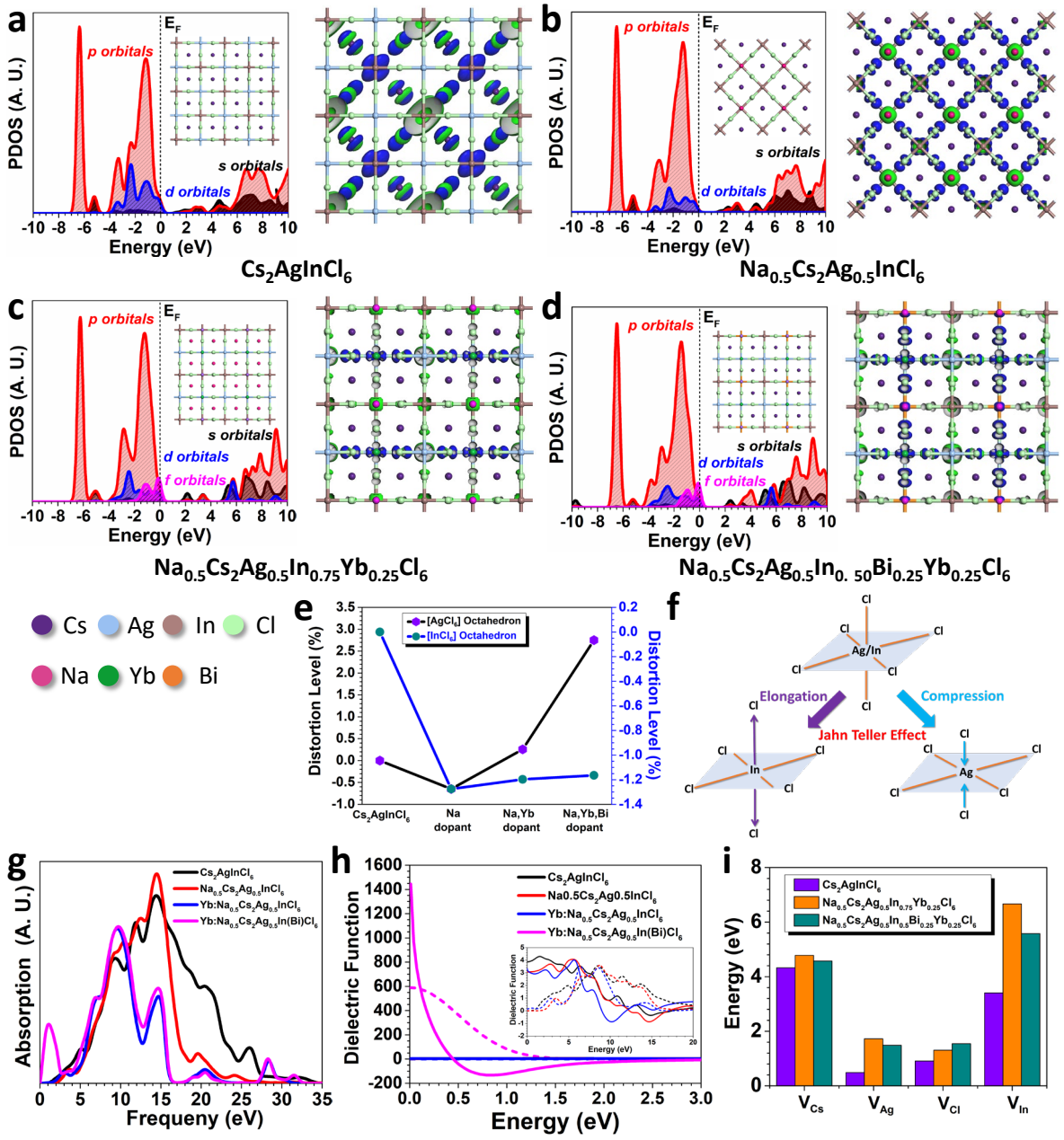

Figure 4. The PDOS, bonding and anti-bonding orbitals of (a) $Cs_2AgInCl_6$, (b) $Cs_2Ag_{0.6}Na_{0.4}InCl_6$, (c) $Cs_2Ag_{0.6}Na_{0.4}InCl_6$:Yb and (d) $Cs_2Ag_{0.6}Na_{0.4}InCl_6$:Yb/Bi. (e) The distortion level of samples (a – d). (f) Schematic illustration of the different Jahn-teller distortion. (g) The simulated absorption spectra. (h) The dielectric function comparison. (i) The vacancy formation energies comparison.

The $Yb^{3+}/Er^{3+}/Bi^{3+}$ co-doped $Cs_2Ag_{0.6}Na_{0.4}InCl_6$ double perovskite material shows the multi-modal luminescence under the excitation of *X*-ray, ultraviolet light and near-infrared laser (980 nm), which also features high stability against humidity and high temperature (up to 400 °C). This luminescence material further extends the functionality and potential for future commercial applications in anti-counterfeiting and X-ray detection.

Keyword Multi-modal Luminescence

Z. Zeng, B. Huang, X. Wang, L. Lu, Q. Lu, M. Sun, T. Wu, T. Ma, J. Xu, Y. Xu, S. Wang, Y. Du* and C.-H. Yan*

Multimodal luminescent $Yb^{3+}/Er^{3+}/Bi^{3+}$-doped perovskite single crystal for X-ray detection and anti-counterfeiting